MEASUREMENT SCIENCE REVIEW, **19**, (2019), No. 3, 109-125

sciendo

ISSN 1335-8871

MEASUREMENT SCIENCE REVIEW

Journal homepage: https://content.sciendo.com

Vibration Detection and Experiment of PMSM High Speed Grinding Motorized Spindle Based on Frequency Domain Technology

Mingke Cheng, Feng Gao[1], Yan Li

Lab. of NC Machine Tools and Integrated Manufacturing Equipment of the Education Ministry & Key Lab of Manufacturing Equipment of Shaanxi Province, Xi'an University of Technology, Xi'an 710048, China. Feng Gao[1], gf2713@xaut.edu.cn

The spindle vibrations of the high-speed grinding motorized spindle largely determine the machining quality and precision. In order to accurately predict the spindle vibrations of the PMSM high-speed grinding motorized spindle, the vibration causes are explored and analyzed. The radial vibration, inclined vibration, and axial vibration model are established. The experimental modal analysis method is proposed to analyze the dynamic response of the spindle and to identify the modal parameters of the spindle structure. Thereafter, the frequency response function (FRF) is calculated by self-power spectrum and cross-power spectrum. It is transformed into the vibration spectrum analysis of the spindle. The least-square method is used to fit the radial trajectory of the spindle. This paper aims to propose double standard spheres for 5-DOF spindle vibrations used to detect the spindle vibrations. In the experiment, the method proposed in this paper can effectively and accurately determine the causes of the spindle vibrations. The spectrum analysis and the trajectory are common tools in the spindle vibration detection.

Keywords: Motorized spindle, vibration analysis, vibration spectrum, trajectory, experiment.

1. INTRODUCTION

The motorized spindle is widely used in large and medium-sized CNC machine tools. The vibration level has become a very important issue in the design and manufacture process [1]-[2]. The axes of the stator and rotor not being coincident are very common in a motorized spindle and the accuracy of a spindle is greatly affected by the bearings. The whirling motion of eccentric rotor, short circuit, demagnetization, magnetization unevenness, and winding asymmetry make the air-gap distorted and a net unbalanced magnetic pull (UMP) on the spindle as consequences. The bearings support the spindle during rotation and sustain the forces exerted by the spindle and external loads. The interaction effect between the electromagnetic field and mechanical structure may cause undesired subcritical resonance vibration of the spindle, and high precision and high efficiency measurement is becoming an imperative requirement for the vibration of the spindle [3].

The motorized spindle vibrations involve many aspects, such as electromagnetic and mechanical. Air-gap eccentricity is one of the causes of the spindle vibrations and also an important feature for detecting vibration signals [4]. The torque, stator current, temperature, inductive, acoustic noises are detected to determine the cause of vibrations. In order to accurately detect the faults and vibrations, in the past several decades several classical methods were proposed. Claudio [5]-[6] et al. used the split-phase currents method to diagnose eccentric rotor in synchronous machines by theoretical analysis and experiments. Hossein et al. proposed a method in which the algorithm is based on the analysis of produced current with a particular variation pattern in switched reluctance motors (SRMs) [7]. Wu et al. used the deviation between the actual value and the desired value of generator no-load electromotive force (EMF) to determine the excitation winding short circuit fault.

The method can achieve higher diagnosis accuracy, and it can be used for the real-time monitoring and diagnosis [8]. Zhang et al. studied the calculations and variations of unbalanced magnetic pull (UMP), of which the excitation source of rotor vibration is the basis and key to online fault monitoring. When the field current is fixed, UMP is negatively correlated with the output active power. When the output active power is unchanged, UMP is positively correlated with the field current [9]. Xie et al. resented a fault diagnosis approach based on the support vector machine (SVM) and they used the principal component analysis (PCA) method and the linear discriminant analysis (LDA) method to solve the high dimensionality for the acquired data. The results show that accuracy of fault diagnosis has improved and cost of SVM training has decreased evidently, and they prove that the proposed approach is practical and

DOI: 10.2478/msr-2019-0017

efficient for fault diagnosis of the rolling bearing system [10]. Glowacz developed and implemented a method of feature extraction of acoustic signals to diagnose the faults of single-phase induction motor [11]. Gritli et al. presented a diagnostic space vector that sensibly improves the rotor fault detection in wound-rotor induction machine by combining the spectral signatures of both rotor current and voltage space vectors [12]. Ibrahim et al.'s proposed approach for rotor electrical asymmetry detection in Wind Turbine DFIGs has been compared with a continuous wavelet transform (CWT) and an iterative localized discrete Fourier-transform (IDFT). The experimental results demonstrate that the CWT and IDFT algorithms fail to track the FSCs at low load operation near-synchronous speed. In contrast, the EKF was more successful in tracking the FSCs magnitude in all operating conditions [13]. Young-Woo Youn et al. proposed a fault diagnosis method that used three phase BEMF voltages based on the fast Fourier transform (FFT), support vector machine (SVM), and visualization tools for identifying fault types and severities in PMSMs. Principal component analysis (PCA) and t-distributed stochastic neighbor embedding (t-SNE) are used to visualize the high-dimensional data into two-dimensional space [14]. However, most of the existing methods with comprehensive theoretical analysis that are based on a stationary assumption (i.e., constant speed and load) are only suitable for fault detection under constant operating conditions. In fact, all these approaches require manual selection of features, which has two issues in real industry applications. First, measurement noise, operator errors, nonlinear dynamics, etc., lead to significant uncertainty in the signal. Second, the number of fault features in collected signal is very large but most of them are distorted or indifferent to health status. Hence, it is difficult to apply in real industrial applications.

Mechanical vibration analysis has been widely used to detect the vibration of a motorized spindle. Generally, feature extraction is the key to vibration detection. The commonly used feature extraction methods can be mainly classified into three categories: the TD analysis, FD analysis, and TD–FD analysis. Time-frequency analysis (TFA), such as short-time Fourier transform [15], wavelet transform, and empirical mode decomposition (EMD) have been widely used in rubbing fault detection [16]. Commonly used detection techniques based on frequency domain (FD) analysis, especially Fast Fourier Transform (FFT) are applied to the dynamic response of the system in order to construct the power spectrum components of the motion [17]. The frequency components contain the rotation frequency, multiplier, and multiplier minus the rotation frequency [18]. Xiang et al. performed FFT to obtain the spectra for the free-motion motion of the permanent magnet synchronous motors. Asymmetric sidebands appear because the amplitude modulations and the phase modulations exist simultaneously [19]. James et al. used FFT analysis to compare the four types of winding connections. The results show that the current redistribution generated by the parallel connections of the windings results in reduction of UMP for IPMSM with eccentricity [20]. Di et al. used FFT results to verify the eccentric model and the theoretical analysis of squirrel cage induction motors [21]. Signals such as current, magnetic flux, mechanical vibration, torque and speed can be analyzed in the frequency domain. There are many methods for collecting the spindle vibration signal, such as a non-contact sensor directly monitoring the vibration displacement; it is also collected by the shell of the motorized spindle. In reality the motorized spindle is more complicated so that the non-contact sensors are difficult to install. In this case, only the indirect measurement methods can be used. Li et al. adsorbed the acceleration sensor on the bearing housing to obtain the displacement curve of the hob spindle [22]. Amirat et al. mounted the sensor on the gearbox to obtain the spindle vibration signal of the fan [23]. Liu et al. analyzed the results showing that the spindle vibrations can be efficient and accurate by measuring the shell vibration [24]. In the above-mentioned methods, the vibration signals of the chassis or the base portion are collected by the sensors as the spindle vibration analysis, but the attenuation of the measurement signal during the transmission process is inevitable. Vibrations of the shaft ending at the joint of the tool cannot be judged. It is difficult to get the spindle motion axis trajectory. Currently, most of the research is only for the radial vibrations of the motorized spindle, but it ignores many other important vibration features, such as the axial vibration and the inclined vibration. 5-DOF spindle vibrations method is rarely used.

The trajectory of the spindle contains very rich information about the motion and has different track in different operating states or vibration faults. Therefore, the trajectory analysis method is a better type of rotating mechanical vibration level identification. The movement trajectory of the rotor is helpful to track the process of the rotor position. It is an important basis for judging whether the system is operating well or not. Xu et al. displayed the trajectory plots of the rotor in the *xy*-plane for different pole-pairs. The rotor comes close to the stator fast and the rub-impact occurs for p=1 and p=2. The trajectory curves for p=3 and p=4 tend to converge gradually and the rub-impact force is not involved [25]. Gu et al. showed journal trajectories at different rotational speeds and studied the effects of dynamic stiffness and damping ratio on stability, unbalance and shock vibration characteristics [26]. Mohammad et al. showed the unbalance trajectories of the nonlinear system to be capable of capturing sub- and super-harmonics [27]-[28]. Xu et al. used the x and y direction motions to study the influence of the motor eccentric force on mechanical vibration stability and nonlinear behavior for induction motor eccentricity [29]. The trajectory plots of the rotor in the plane of the healthy motor or faulty motor are similar to a circle or an ellipse. The trajectory is determined by many factors, such as nonlinear vibration, bearings and so on. There are different causes for vibration problems in the motorized spindle. Studying the trajectory is useful for understanding and mastering the motion of the spindle. Different trajectory results in a different spindle vibration. Hence, it can be used to be an important basis for the vibration detection of the motorized spindle, and it has the advantages of simplicity, intuitiveness, and easy judgment of faults.

Aiming at the vibration problems generated during the trial run of the PMSM, grinding motorized spindle was developed by a machine tool factory. Many factors have significant influence on the spindle vibrations, radial, inclined, and axial vibration models. Experimental modal method is used to identify the modal parameters. The self-power spectrum and cross-power spectrum are used to obtain the frequency response function of the spindle vibrations and the double spheres for 5-DOF spindle vibrations can be detected in all directions. Firstly, a radial vibration model under the spindle rotation is proposed, and the trajectory is synthesized according to the radial vibration displacement. Then, an inclined vibration model is proposed based on the radial vibration analysis method to obtain the tilting angle. The axis vibration curve is analyzed and a method for evaluating the axial vibration is given by the TD and FD methods. Finally, the spindle vibration analysis method is applied to the PMSM grinding motorized spindles of type YKZ7230 and YKS7225. The vibration characteristics are analyzed and evaluated.

2. THE SOURCES OF MOTORIZED SPINDLE VIBRATIONS

UMP is usually generated by the distorted air-gap field of an eccentric rotor and the spindle bearing system is one of the most important parts of a machine tool. They directly affect the performance of the machine tool [30]. Therefore, a thorough understanding of spindle vibrations is of great significance in making full use of the spindle system and in improving productivity. The spindle radial vibration, axial vibration, and inclined vibration are shown in Fig.1.

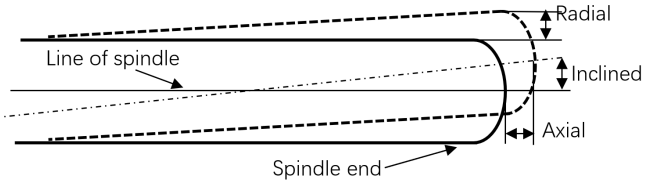

Fig.1. Schematic diagram of spindle vibrations.

A. Electromagnetic vibration

The electromagnetic vibration is directly related to the uneven air-gap that causes the UMP. The mechanical cause of the UMP is mainly the air-gap eccentricity between the stator and the rotor. Fig.2. shows the sources of air-gap eccentricity that can be divided into four categories: shape deviation, parallel eccentricity, inclined eccentricity, and curved eccentricity.

Fig.3. shows that the rotor and stator axes are parallel, the air-gap eccentricity can be divided into three categories: static (SE), dynamic eccentricity (DE), and mixed eccentricity (ME) [31]. ME is the SE and DE mixed eccentricity, that is SE and DE coexist. The radial centrifugal force is generated during the rotation of the motorized spindle, which results in the uneven air-gap. The SE is easily caused by the installation parallel deviation and bearing wear. ME can be regarded as the SE plus the DE.

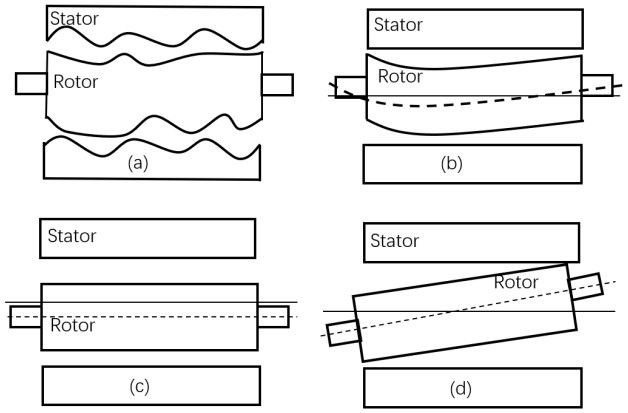

Fig.2. The main mechanical sources of air-gap eccentricity: a) shape deviation, b) parallel eccentricity, c) inclined eccentricity, and d) curved eccentricity.

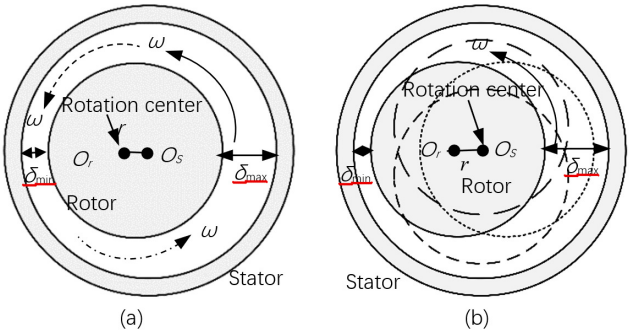

Fig.3. Two common cases of parallel eccentricity: a) static eccentricity and b) dynamic eccentricity.

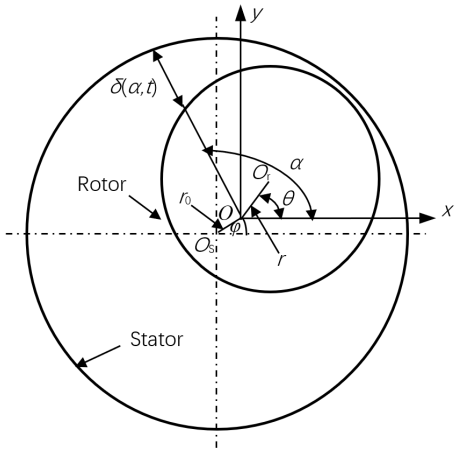

Fig.4. Schematic diagram of static and dynamic mixed eccentricity.

The air-gap length is greatly important to the calculation of the UMP and the vibration analysis of the spindle. As Fig.4. shows, the geometrical centers of the stator and rotor are the O_s, O_r, and the initial geometrical center of rotor is O. The air-gap length for ME can be approximately expressed by equation as follows [32]:

$$\delta(\alpha,t)\approx\delta_0-r_0\cos(\alpha-\varphi)-r\cos(\alpha-\theta) \quad (1)$$

Where r_0 is the SE; r represents the DE; δ_0 is the average air-gap length when the rotor is at center; α is the air-gap angle with reference to the x-axis; φ and θ are the angles of SE and the DE with reference to the x-axis, respectively.

The air-gap lengths of the SE and DE are, respectively, as follows:

$$\delta(\alpha,t)\approx\delta_0-r_0\cos(\alpha-\varphi) \quad (2)$$

$$\delta(\alpha,t)\approx\delta_0-r\cos(\alpha-\theta) \quad (3)$$

In engineering practice, height between the bearings on both sides of the rotor shaft and the inclination of the shaft, etc., causes the air-gap differences at different positions along the axial direction. This eccentricity is named inclined eccentricity, as shown in Fig.5. The air-gap eccentricity is related to the inclined angle and axial position of the rotor.

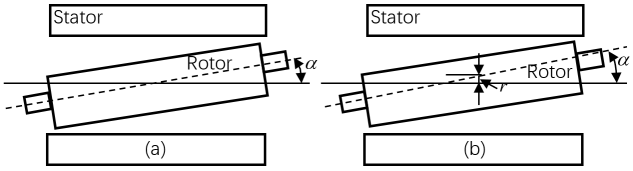

Fig.5. Schematic diagram of inclined eccentricity: a) symmetrical eccentricity and b) both static and inclined eccentricity.

It is assumed that the stator is stationary and the midpoint of the rotor in the axial direction is selected to be the origin of the coordinates. There exist two orthogonal coordinate systems of three-dimensional space and they are parallel, as shown in Fig.6., where *O-XYZ* is stationary coordinate system of the stator and *o-xyz* is the unfixed coordinate system of the rotor. The comprehensive eccentricity of the investigated cross section is:

$$r_0=\sqrt{\left[x_0+Z\cos\left(\theta_{x0}+\theta_x\right)\sin\left(\theta_{y0}+\theta_y\right)\right]^2+\left[y_0-Z\sin\left(\theta_{x0}+\theta_x\right)\right]^2} \quad (4)$$

$$\varphi=\begin{cases}\arccos\dfrac{x_0+Z\cos(\theta_{x0}+\theta_x)\sin(\theta_{y0}+\theta_y)}{r_0} & y_0-Z\sin(\theta_{x0}+\theta_x)\ \geq 0\\ 2\pi-\arccos\dfrac{x_0+Z\cos(\theta_{x0}+\theta_x)\sin(\theta_{y0}+\theta_y)}{r_0} & y_0-Z\sin(\theta_{x0}+\theta_x)\ <0\end{cases} \quad (5)$$

Where Z is the intersection point between the investigated cross section and the *OZ*-axis.

The common range of φ is [0, 2π], while the scope of inverse trigonometric functions is [0, π]. The following extension is conducted [33]:

The air-gap length in an arbitrary cross-section can be approximately expressed by an equation as follows:

$$\delta(\alpha,t,z)=\delta_0-r_0\cos(\alpha-\varphi)-r\cos(\alpha-\theta) \quad (6)$$

The air-gap length in an arbitrary cross-section can be approximately expressed by an equation as follows:

$$z=Z\cos(\theta_{x0}+\theta_x)\sin(\theta_{y0}+\theta_y)\ Z\in\left(-\frac{L}{2},\frac{L}{2}\right) \quad (7)$$

Where L is the axial length of air-gap.

To calculate the UMP at different positions, a multilayer model has been developed when there is bending eccentricity. The shaft is divided into several layers along the axial direction from one side of the motor shaft to the spindle. These layers are numbered from 1 to N, as shown in Fig.7. Each layer is assumed to be at a certain level of eccentricity, and different layers show different eccentricity degrees [21].

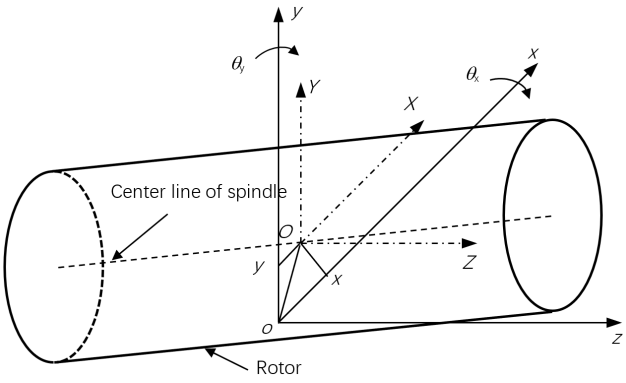

Fig.6. Schematic diagram of mixed inclined eccentricity.

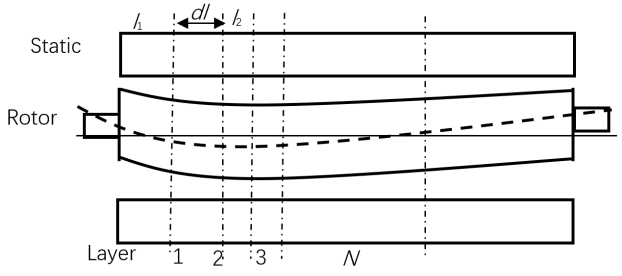

Fig.7. Schematic diagram of the curved eccentricity.

To sum up, air-gap eccentricity types between them are summarized in Fig.8.

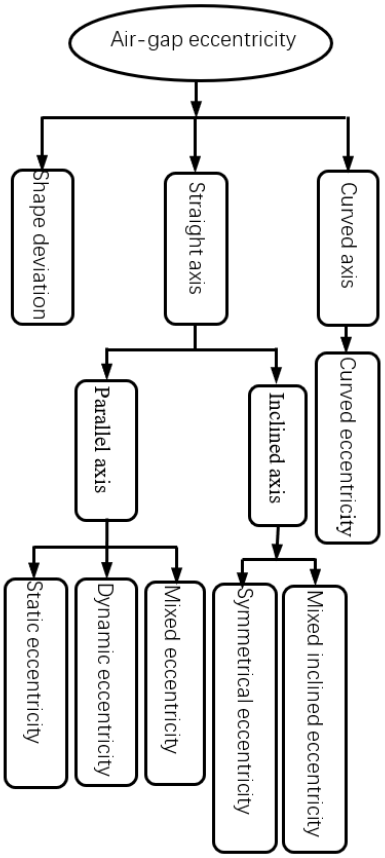

Fig.8. Summary of different air-gap eccentricity types.

The electromagnetic aspects can be summarized in four categories: short circuit, open circuit, magnetization unevenness, and winding topology asymmetry. The most common problem is the short circuit which occurs in the stator slot, the magnetic flux of the air-gap changes. The UMP results in radial vibration. The reasons for short circuits can be electrical, mechanical, thermal, environmental, etc. The common types of short circuit are turn-to-turn, coil-to-coil, phase-to-phase, and phase-to-ground short circuit. Dielectric, corona discharge, leakage traces and transient voltage are some of the electrical stresses that cause the short circuit. The magnetization unevenness is manifested in the phenomenon where demagnetization occurs. Especially in the high torque state, the reverse magnetic field generated by the stator current resists the residual magnetic induction of the permanent magnet. The factors that cause magnetization unevenness can be divided into non-uniform magnetization of permanent magnet materials and magnetization of soft magnetic materials. The reverse magnetic field generated by the stator current resists the residual magnetic induction of the permanent magnet, especially when it causes the rotor magnet demagnetization under high torque operation and high temperatures. The open circuit can also make the magnetic circuit unequal. This leads to unbalanced magnetic flux. Electromagnetic sources are also the main reasons for the UMP.

B. Mechanical vibration

Fig.9. shows the schematic of an angular contact bearing. Spindle vibrations due to bearing are an issue that has drawn an increasing industrial interest over recent years. The ball-bearings supporting the spindle vibrations are categorized into three types, namely inner ring, outer ring, and ball damages. These vibrations affect the air–gap eccentricities which perturb flux density [34].

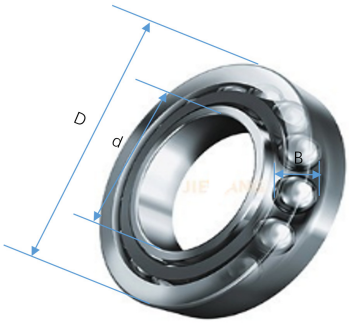

Fig.9. Rolling bearing dimensions.

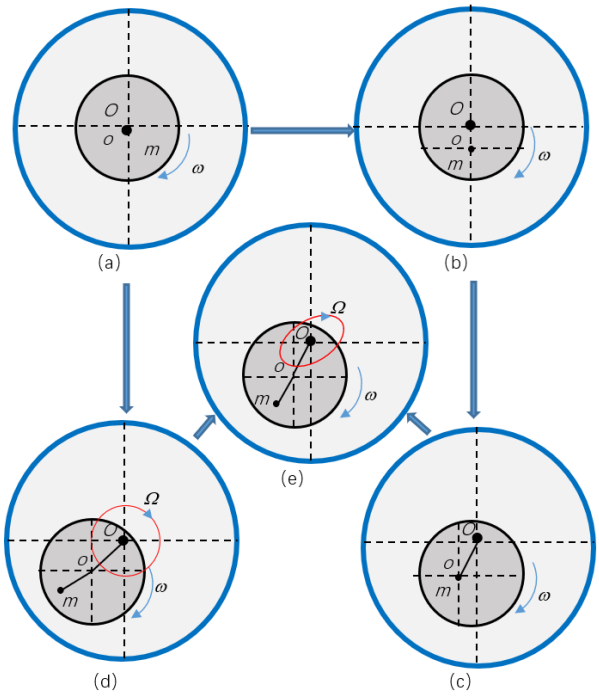

Fig.10. Illumination of spindle motion: a) ideal case, b) eccentricity, c) bearing hydrodynamics, d) inertial effect, and e) actual case.

In order to avoid the bearing burn out caused by the high-speed running, the system usually has a gap between the bearing inner ring and the shaft, which will cause the spindle vibrations and affect the spindle motion [35]. Fig.10.a) shows that the spindle runs around its bearing center without bearing dynamics and inertial effect under an ideal case. Fig.10.b) displays the spindle deviation from the bearing center due to gravity. Additionally, nonlinear Hertz contact force further makes the spindle diverge as shown in Fig.10.c). Thereafter,

a new equilibrium center/axis occurs and remains static. Under inertial effect (inertial force and inertial moment) induced by mass eccentricity the spindle rotates around the bearing center with an eccentricity and a tilting angle. Result in whirling/tilting/precession effect arises. Hence, spindle whirling and spindle tilting occurs. Furthermore, the spindle rotation keeps pace with the revolution, i.e., $\omega=\Omega$. However, the spindle orbit is still circular as demonstrated in Fig.10.d). Resultantly, the spindle whirling and spindle tilting are not circular but synchronous and quasi-elliptical as exhibited in Fig.10.e).

3. VIBRATIONS DETECTION ANALYSIS

A. Radial vibration detection

The standard spheres are mounted on the spindle end and the displacement sensors are mounted in two radial directions which are mutually perpendicular to collect the radial vibration displacement curve of the spindle, as shown in Fig.11. [36].

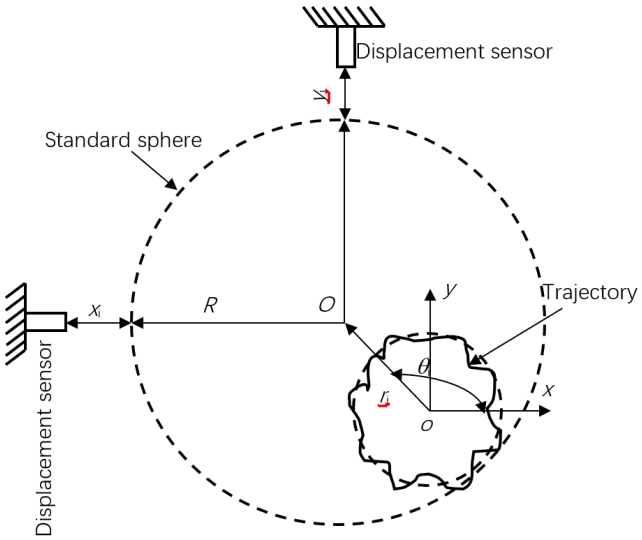

Fig.11. Schematic diagram of radial vibration detection.

In the figure, O represents the geometrical center of the standard sphere. o represents the average line of the spindle at the radial motion. Radial horizontal direction is represented by the x-axis, the radial vertical direction by the y-axis, and the axial direction by the z-axis. By the geometric relationship the radial displacements are given by the following equations:

$$x_i = |X_1| - r_i \cos\theta_i - \sqrt{R^2 - \left(|Y_2| + r_i \sin\theta\right)^2} \quad (8)$$

$$y_i = |Y_1| - r_i \sin\theta_i - \sqrt{R^2 - \left(|X_2| + r_i \cos\theta\right)^2} \quad (9)$$

Where r_i is the superimposed length of the standard sphere eccentricity and the radial displacement of the spindle, i.e., $r_i=|oO|$; R is the radius of the standard sphere; x_i and y_i are the displacement signals of the standard sphere along the x and y directions, respectively; Y_1 and Y_2 represent the distance between the two displacement sensors and the center of the spindle along the y axis, respectively; X_1 and X_2 represent the distance between the two displacement sensors and the center of the spindle along the x axis, respectively.

B. Inclined vibration detection

The inclined vibration can be expressed by the tilting angle and the model is based on a radial vibration [37]. Fig.12. shows that the radial displacement curves of the outer standard ball and the inner standard are collected by four displacement sensors.

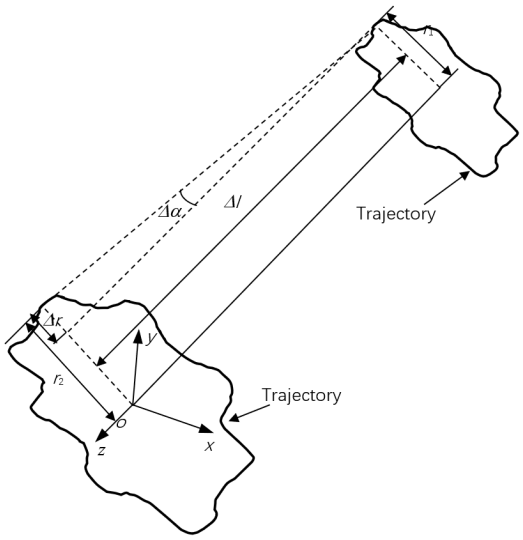

Fig.12. Schematic diagram of inclined vibration detection.

In the figure, o represents the axial average line of the spindle, $\Delta\theta$ represents the tilting angle, r_1 and r_2 represent the radial displacement, respectively, and Δl represents the distance of the inner standard sphere from the outer standard sphere. The tilting angle of inclined vibration is defined by:

$$\Delta\alpha = \arctan\frac{\Delta r}{\Delta l} = \arctan\frac{r_2 - r_1}{\Delta l} \quad (10)$$

C. Axial vibration detection

The axial vibration is detected by a displacement sensor which is mounted on the front end of the double standard sphere, as displayed in Fig.13. [38]. It can be seen that the center of the spindle and the standard sphere center are not coincident, and the eccentricity must be separated first. The signal of the eccentricity is a periodic signal with a cycle of the rotational speed. However, the set speed and the actual speed are not completely consistent, it is necessary to perform FFT transformation on the collected displacement signal to obtain the frequency. Non-zero frequency of the largest amplitude is the rotation frequency as follows:

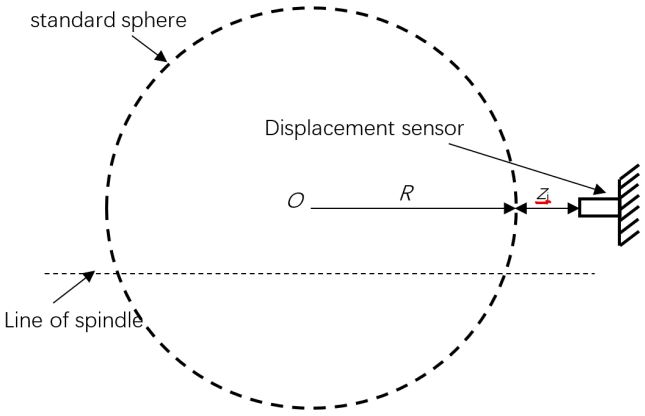

Fig.13. Schematic diagram of axial vibration detection.

$$D(f)=\max\left(DTFT\left[z_i\right]\right)=\sum_{i=-\infty}^{\infty} z_i e^{-j\omega i} \qquad (11)$$

Where *DTFT* represents discrete Fourier transform, f represents the main frequency of the axial motion, and $D(f)$ represents the amplitude of the actual rotational frequency.

4. FREQUENCY DOMAIN (FD) ANALYSIS

A. Bearing-rotor model

Fig.14. shows a typical motorized spindle rotor and bearing configuration. The PMSM motorized spindle is designed with high power density, light weight miniaturization and wide range speed regulation. Therefore, the structure is complex and the rigidity is low. The spindle vibrations are very complicated, involving electromagnetic and mechanical aspects.

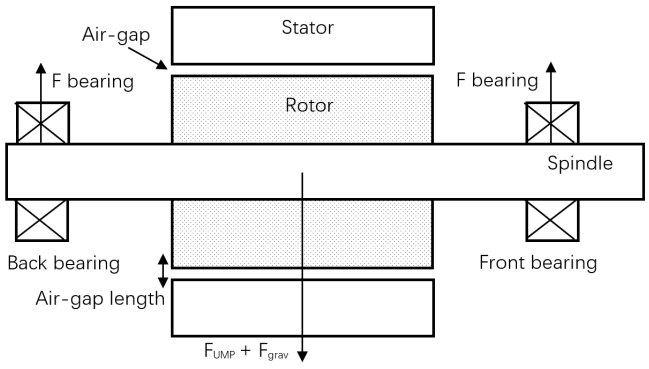

Fig.14. Motorized spindle configuration.

Further, taking into consideration that the rotational frequency (corresponding to spindle speed ω) under electromagnetic and mechanical aspects would excite the spindle vibrations, the natural frequencies of the employed spindle should be identified. In order to simplify the model motorized spindle rotor and bearing, Timoshenko beam and Finite Element (FE) theory are used for the idealized geometric and physical assumptions. The bearing-rotor model is given by the following equation:

$$[M]\{\ddot{X}\}+[C]\{\dot{X}\}+[K]\{X\}=\{f(t)\} \qquad (12)$$

Where $[M]$ is the mass matrix, $[C]$ is the damping matrix, and $[K]$ is the stiffness matrix.

B. Experimental modal analysis method

It is assumed that the spindle was driven by a motorized spindle; the excitation and the response signal were measured to obtain the frequency response function (FRF) between the excitation point and the spindle. In general, the first few modes are used to analyze the dynamic characteristics of the spindle. Therefore, it is necessary to convert the dynamic model in physical coordinates to the modal coordinates. It is simple and effective to solve the model after the reduced order.

Fourier Transformation (FT) of the equation (15) is as follows:

$$\left(-\omega^2[M]+j\omega[C]+[K]\right)\{X(\omega)\}=F(\omega) \qquad (13)$$

Where $X(\omega)$ and $F(\omega)$ are the FT of $X(t)$ and $F(t)$, respectively, which are both functions of ω, also known as the FT of force and response.

Because the sensors are not mounted on the object, they do not change the object's mass or its resonant characteristics. These sensors have a flat frequency response from DC to near their rated frequency response. However, the output is not affected by the frequency of the vibration, measurements are more accurate across the frequency spectrum. The above equation can be abbreviated as:

$$\left[Z(\omega)\right]\{q(\omega)\}=\{F(\omega)\} \qquad (14)$$

Where $Z(\omega)$ is the impedance matrix.

After both ends of equation (14) are multiplied by the inverse of the impedance matrix.

$$\{x(\omega)\}=\{H(\omega)\}\{F(\omega)\} \qquad (15)$$

Where $H(\omega)$ is the admittance matrix, which is the inverse of the impedance matrix $Z(\omega)$ and the n-order symmetric matrix.

Equation (15) is expanded in the Lth row:

$$X_l=H_{l1}F_1+H_{l2}F_2+\cdots+H_{lp}F_p+\cdots+H_{\ln}F_n \qquad (16)$$

When the force of the other points is zero on the test structure, the complex ratio of the l-point response spectrum to the p-point excitation spectrum is conducted:

$$H_{lp}(\omega)=\frac{X_l(\omega)}{F_p} \qquad (17)$$

Equation (17) reflects the transmission path of the excitation energy, and the response characteristics can be illustrated under the excitation force. Admittance matrix has symmetrical property, $H_{ij}= H_{ji}$, that is, the i-point is completely consistent with the admittance of the j-point. The one row or one column elements can be used to determine the entire admittance matrix.

For the bearing-rotor dynamics model, the physical coordinates were linearly transformed in equation (12).

$$\{x\} = [\phi]\{q\} \tag{18}$$

Where $[\Phi]$ is composed of arrays of various modes.

Substituting equation (18) into equation (12):

The transposition of the left-multiplied mode matrix at both ends is:

The mode matrix, the mass matrix, the stiffness matrix and the damping matrix with orthogonal properties are diagonalized.

$$[M][\phi]\{\ddot{q}\} + [C][\phi]\{\dot{q}\} + [K][\phi]\{q\} = \{f\} \tag{19}$$

$$[\phi]^T [M][\phi]\{\ddot{q}\} + [\phi]^T [C][\phi]\{\dot{q}\} + [\phi]^T [K][\phi]\{q\} = [\phi]^T \{f\} \tag{20}$$

$$\begin{pmatrix} \backslash & & \\ & m_i & \\ & & \backslash \end{pmatrix}\{\ddot{q}\} + \begin{pmatrix} \backslash & & \\ & c_i & \\ & & \backslash \end{pmatrix}\{\dot{q}\} + \begin{pmatrix} \backslash & & \\ & k_i & \\ & & \backslash \end{pmatrix}\{q\} = [\phi]^T \{f\} \tag{21}$$

There are n single-degree-of-freedom differential equations all by oneself, where the i-th equation is

$$m_i\ddot{q} + c_i\dot{q} + k_i q_i = \sum_{j=1}^{n} \varphi_{ji} f_i \tag{22}$$

Let the solution be $q_i=Q_i e^{j\omega t}$ to solve the amplitude

$$Q_i = \frac{\varphi_{pi} F_p}{k - \omega^2 m_i + j\omega c_i} \tag{23}$$

The response amplitude should be

$$X_i = \sum_i \varphi_{li} Q_i \tag{24}$$

Substituted equation (24) into equation (23), the response amplitude of the l-point can be determined as follows:

$$X_l = \sum_{i=1}^{n} \frac{\varphi_{li}\varphi_{pi}}{k_i - \omega^2 m_i + j\omega c_i} \tag{25}$$

The entire admittance matrix can be calculated as

$$[H] = \sum_{i=1}^{n} \frac{\{\varphi\}_i \{\varphi\}_i^T}{k_i - \omega^2 m_i + j\omega c_i} \tag{26}$$

The dynamic characteristics of the system are determined.

The displacement-admittance of the point p to any point l is as follows:

$$\left|H_{lp}(\omega)\right| = \left|\sum_{i=1}^{N} \frac{\left(D_{lp}\right)_i}{1 - \left(\frac{\omega}{\omega_i}\right)^2 + 2j\xi_i \frac{\omega}{\omega_i}}\right| \approx \frac{\left(D_{lp}\right)_r}{\sqrt{\left[1 - \left(\frac{\omega}{\omega_i}\right)^2\right]^2 + 4\xi_r^2 \left(\frac{\omega}{\omega_i}\right)^2}} \tag{27}$$

Where ξ_r is the r-order modal damping ratio, $\xi_r=\Delta\omega/\omega_r$; ω_r is the r-th natural frequency.

As $\omega=\omega_r$:

$$\left|H_{lp}(\omega_r)\right| = \frac{\left(D_{lp}\right)_r}{2\xi_r} \tag{28}$$

$$\left(D_{lp}\right)_r = \frac{\varphi_{lr}\phi_{pr}}{k_r} \tag{29}$$

Let Φ_{pr}=1, *r*-order mode stiffness and mode can be calculated as

$$k_r = \frac{1}{2\xi_r \left| H_{lp}(\omega_r) \right|} \tag{30}$$

$$\{\phi_r\} = \begin{Bmatrix} \phi_{1r} \\ \phi_{2r} \\ \cdots \\ \phi_{lr} \end{Bmatrix} = \begin{Bmatrix} \pm\left| H_{1p}(\omega_r) \right| \\ \pm\left| H_{2p}(\omega_r) \right| \\ \cdots \\ \pm\left| H_{lp}(\omega_r) \right| \end{Bmatrix} \tag{31}$$

C. Frequency response function (FRF) calculation

The spectra of the input and the output signals are *F*(*f*) and *x*(*f*), respectively. Then the FRF is

$$H(f) = \frac{X(f)}{F(f)} \tag{32}$$

A calculation of the self-power and mutual-power spectrum to solve mechanical admittance and FRFs is converted to spectrum analysis.

$$H_1(f) = \frac{X(f)F^*(f)}{F(f)F^*(f)} = \frac{G_{XF}}{G_{FF}} \tag{33}$$

$$H_2(f) = \frac{X(f)^* X(f)}{F(f)X^*(f)} = \frac{G_{XX}}{G_{FX}} \tag{34}$$

Where ∗ represents conjugate symbol.

In time, the average of the self-power and the cross-power spectrum can be described by

$$\hat{G}_{FF} = \frac{1}{N}\sum_{n=1}^{N_a}(G_{FF})_n \tag{35}$$

$$\hat{G}_{XX} = \frac{1}{N}\sum_{n=1}^{N_a}(G_{XX})_n \tag{36}$$

$$\hat{G}_{FX} = \frac{1}{N}\sum_{n=1}^{N_a}(G_{FX})_n \tag{37}$$

$$\hat{G}_{XF} = \frac{1}{N}\sum_{n=1}^{N_a}(G_{XF})_n \tag{38}$$

Where N_a is the average number.

The least-square approximation of *H*(*f*) is used to estimate the FRFs of the spindle.

D. Trajectory of the spindle motion model

In order to better represent the vibration-displacement signals, it is necessary to remove the offsets of x_i and y_i and transform the equations (11) and (12) as follows:

$$x_i^{'} = x_i - \frac{\sum_{i=1}^{n} x_i}{n} \tag{39}$$

$$y_i^{'} = y_i - \frac{\sum_{i=1}^{n} y_i}{n} \tag{40}$$

Where $x_i^{'}$ and $y_i^{'}$ are the displacement signals after the offset is removed; *n* is the number of detections.

Referencing the Chinese National Standard GB17421-7-2016, the radial vibration-displacement of the spindle is analyzed by the least-square method. The formula of the least-square circle is

$$\sum_{i=1}^{n}\varepsilon_i^2 = \sum_{i=1}^{n}\left(\sqrt{(x_i - x_0)^2 + (y_i - y_0)^2} - r_{\min}\right) \tag{41}$$

Where x_0 and y_0 are the abscissa and ordinate of the least-square circle, respectively; $r_{\min}$ is the radius of the least-square circle.

It is minimized $\sum_{i=1}^{n}\varepsilon_i^2$ by solving x_0 ,y_0, and $r_{\min}$. Since the least-square method has no analytical solutions, considering the accuracy and efficiency, the equation (41) can be approximately described by

$$H = \sum_{i=1}^{n}\left[(x_i - x_0)^2 + (y_i - y_0)^2 - r_{\min}^2\right] \tag{42}$$

The final calculation can be approximately expressed as follows [36]:

$$x_0 = -\frac{t_1}{2} \tag{43}$$

$$y_0 = -\frac{t_2}{2} \tag{44}$$

$$r_{\min} = \sqrt{\frac{t_1^2}{4} + \frac{t_1^2}{4} - t_3} \tag{45}$$

Where $t_1 = \dfrac{A_1 A_5 - A_3 A_4}{A_3^2 - A_2 A_5}$, $t_2 = \dfrac{A_1 A_3 - A_4 A_4}{A_2 A_5 - A_3^2}$,

$$t_3 = -\frac{\sum_{i=1}^{n}\left(x_i^2 + y_i^2 + t_1 x_i + t_2 y_i\right)}{n},$$

$$A_1 = \sum_{i=1}^{n}\left[\left(x_i^2 + y_i^2\right)x_i\right] - \frac{1}{n}\sum_{i=1}^{n}\left(x_i^2 + y_i^2\right)\sum_{i=1}^{n} x_i ,$$

$$A_2 = \sum_{i=1}^{n} x_i^2 - \frac{1}{n}\sum_{i=1}^{n} x_i \sum_{i=1}^{n} x_i ,$$

$$A_3 = \sum_{i=1}^{n} x_i y - \frac{1}{n}\sum_{i=1}^{n} x_i \sum_{i=1}^{n} y_i ,$$

$$A_4 = \sum_{i=1}^{n}\left[\left(x_i^2 + y_i^2\right)y_i\right] - \frac{1}{n}\sum_{i=1}^{n}\left(x_i^2 + y_i^2\right)\sum_{i=1}^{n} y_i ,$$

$$A_5 = \sum_{i=1}^{n} y_i^2 - \frac{1}{n}\sum_{i=1}^{n} y_i \sum_{i=1}^{n} y_i .$$

The center of the radial vibration-displacement curve of the spindle at different rotational speeds is calculated by the least-square algorithm.

E. Vibration detection

Table 1. shows that the most common causes of the spindle vibrations can be divided into three categories: rotor, bearing, and electrical machinery. There are four reasons for rotor vibration: rotor imbalance, rotor bending, rotor misalignment, and rotor looseness, which can be detected and analyzed by FD techniques [39].

The frequences cluster generated due to ball-bearings is given by the following equations:

$$f_o = \frac{Z}{2} f_r \left(1 - \frac{d}{D}\cos\alpha\right) \tag{46}$$

$$f_i = \frac{Z}{2} f_r \left(1 + \frac{d}{D}\cos\alpha\right) \tag{47}$$

$$f_b = \frac{Z}{2} f_r \left(1 - \frac{d^2}{D^2}\cos^2\alpha\right) \tag{48}$$

Table 1. Types of motorized spindle vibrations and their corresponding characteristic frequency spectra.

Vibrations region	Vibration causes	Frequency spectrum
Rotor	Rotor imbalance	1*f* exhibits the highest peak value,and the other harmonic frequencies are extremely small.
	Rotor bending	The frequency spectra appear at 1*f* , 2 *f* , and *3f* and descend gradually.
	Rotor misalignment	2 *f* exhibits the highest spectral value; 1*f* and 3*f* have spectral values slightly lower than that of 2 *f* ; 4 *f* also features a spectral value.
	Rotor looseness	The spectral values of 1 *f* , 2 *f* , and 3 *f* are substantial and descend gradually; fraction number multiplier frequency values also appear
Bearing	Inner ring damage	A frequency cluster appears in the form of $f_i \pm n f_\omega$(m=1,2,3…;n=0,1,2,…).
	Outer ring damage	A frequency cluster appears in the form of $m f_o \pm n f_{cage}$(m=1,2,3…;n=0,1,2,…)
	Ball damage	A frequency cluster appears in the form of $m f_i \pm n f_{cage}$(m=1,2,3…;n=0,1,2,…)
Electric machinery	Static eccentricity	A frequency cluster is generated at *nf* （n=1,2,3…）
	Dynamic eccentricity	A frequency cluster is generated at 1*f*
	Rotor damper winding	A frequency cluster is generated at 1*f* 、 2 *f*、 $f_b \pm nN_r$(n=1,2,3…)
	Phase imbalance	The frequency spectrum in 6 f_L is the most substantial, and a frequency spectrum also appears at 1*f*.

Where，f_r represents the bearing rotational frequency; f_0 ,f_i represent the frequency when the ball passes the initial point of the outer ring and inner ring, respectively , f_b represents the frequency of balls passing through the outer or inner rings, D represents the pitch diameter, d represents the ball diameter, Z represents the number of balls, and α represents the contact angle.

In the light load (less than 50 %) conditions, it can be distinguished from the beginning to experience different degrees of vibration by the mechanical vibration spectrum.

In order to detect the spindle vibrations at one time, a double-standard sphere and displacement sensors are used to build an experimental platform and the vibration signals are collected as shown in Fig.15.

Firstly, the standard sphere is mounted on the front end of the spindle, then the two displacement sensors are mounted on the inner standard ball in the radial vertical direction and the radial horizontal direction, respectively, and also the displacement sensors are installed on the outer standard sphere in the same directions. In the two detection directions, one displacement sensor is finally mounted on the outer standard sphere in the axial direction. The radial displacement of the outer standard sphere is detected by two displacement sensors and the radial displacement signal of the spindle is collected. The radial displacement of the inner and the outer standard sphere are detected by four sensors and the inclined signal is collected. The axial displacement of the outer standard sphere is detected by a sensor and the axial signal is collected. Fig.16. shows the flow chart of the spindle vibration detection.

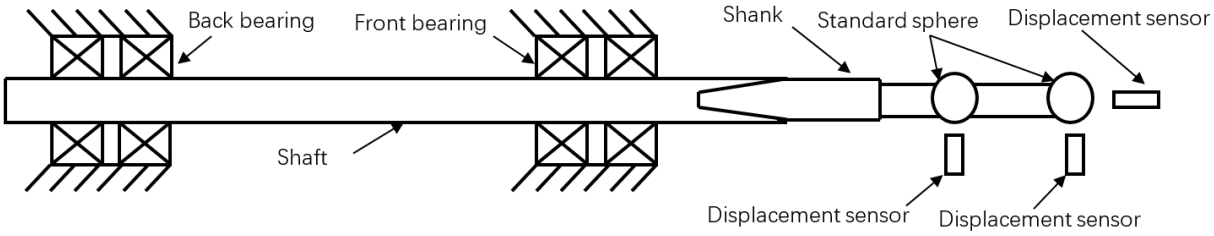

Fig.15. Principle of the spindle vibrations detection.

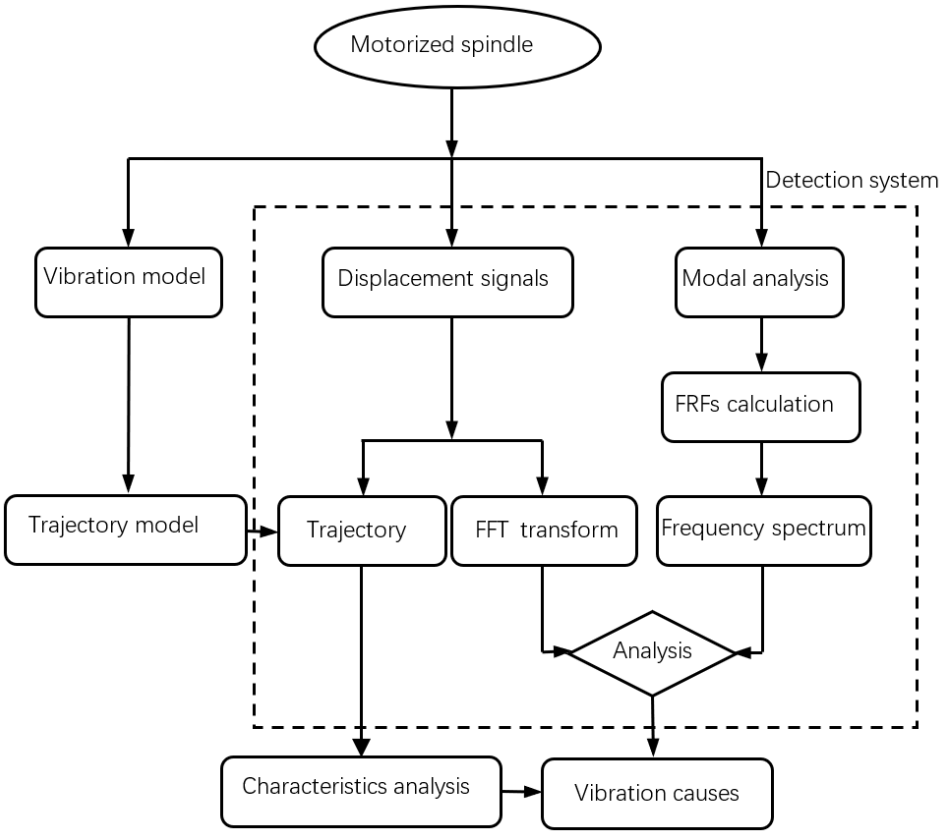

Fig.16. Flow chart of the spindle vibrations detection.

4. EXPERIMENTAL SET-UP

The experiments were performed on two PMSM grind motorized spindles which were manufactured by a machine tool company in China. Their models are YKZ7230 and YKS7225, respectively and the parameters are presented in Table 2. This paper used the MSSS-2556 testing system and the Lion non-contact capacitive displacement sensors to measure the displacement response of the standard sphere at the end of the spindle. The experiment setup is shown in Fig.17.

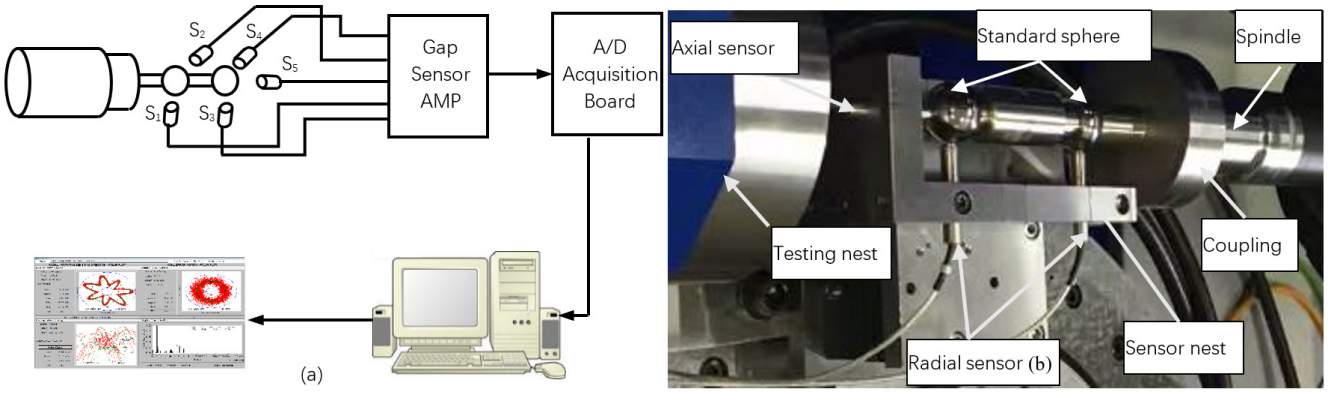

Fig.17. Data acquisition system: a) Typical testing set-up for 5-DOF spindle vibrations and b) Experimental setup.

Table 2. Motorized spindle parameters.

Parameter	**YKZ7230**	**YKS7225**
Phase	3	3
Pole-pair	3	2
Rated power /Kw	25	11.5
Mass of the stator /Kg	22.9	6
Mass of the rotor /Kg	4.3	0.57
Outer diameter of the stator /mm	116	93
Inner diameter of the stator /mm	84.2	55.1
Outer diameter of the rotor /mm	83.2	54.5
Inner diameter of the rotor /mm	58	44
Length of the stator and rotor /mm	200	117
Length of the spindle /mm	517	157
Inertia of the rotor /r²	0.021	0.00033

5. DISCUSSION

Following the proposed method, the characteristic frequencies were measured at the different speeds for the model YKZ7230 motorized spindle. The speeds were n=3200 rpm, n=3500 rpm, n=3600 rpm, n=3800 rpm, n=4000 rpm, n=4200 rpm, n=4500 rpm, n=4800 rpm, and n=5000 rpm, respectively. The aim was to identify the spindle vibrations. Such characteristics can be found by measuring the spindle frequencies for different spindle speeds as it is illustrated in Fig.18. From the spectrum results, it can be asserted that the 6 rev.$^{-1}$ is the harmonics of 2 rev.$^{-1}$,7 rev.$^{-1}$ is the harmonics of 1 rev.$^{-1}$. That was induced by nonlinear Hertz contact force induced forced spindle vibrations, since their amplitude gradually decreases and their maximum amplitude is 6 rev.$^{-1}$. They equally correspond to the bearing inner ring caused eccentricity between bearing and shaft of the spindle. The 6 rev.$^{-1}$ and 12 rev.$^{-1}$are the harmonics of 6 rev.$^{-1}$. They correspond to the fundamental cyclic frequency of UMP induced forced spindle vibration equal to the magnetic poles of the spindle motor 2p and there are 1st and 2nd harmonics, obviously corresponding to the bearing inner ring damage and the eccentricity frequencies of the employed spindle. The UMP generated by the eccentricity and spindle imbalance force caused the radial vibration. The maximum amplitude of the vibration reaches 4.3 μm at n=4500 rpm. Therefore, it can be inferred that the UMP was constant and that the centrifugal force gradually increased, the amplitude of the spindle vibrations was decreased as the rotation speed increased. It is shown that the effect of mass eccentricity was more obvious.

Fig.19. shows the measured trajectories for five different rotational speeds. In all the cases, the trajectories gradually transition from an approximate ellipse to a petal state. It is evident that at different rotational speeds UMP and mass

eccentricity cause the spindle to fluctuate more during the motorized spindle operation. The rotationally sensitive direction errors increased from 4.41 μm to 15.03 μm with increasing rotational speed. However, the sensitive direction error is smaller than 3.21 μm in axial direction at n=4680 rpm as portrayed in Fig.20.

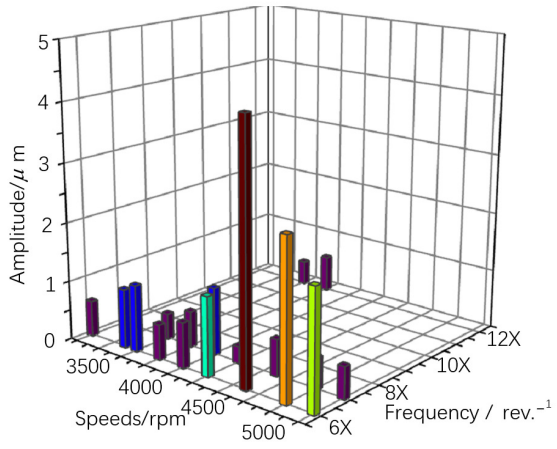

Fig.18. Measured vibration signals spectrum.

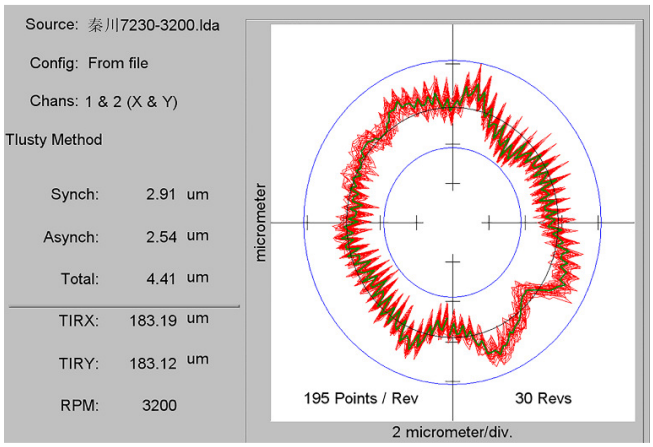

a)

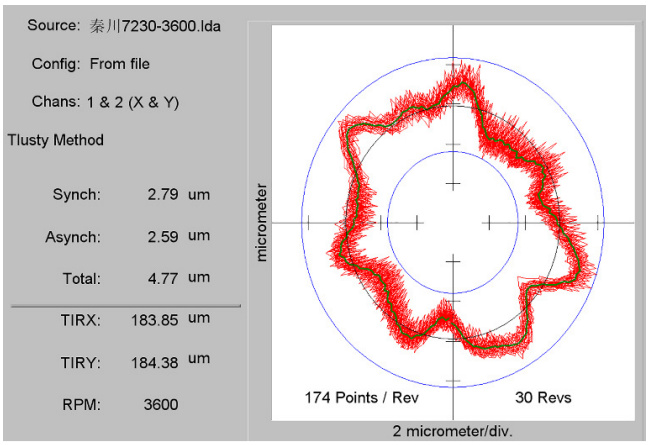

b)

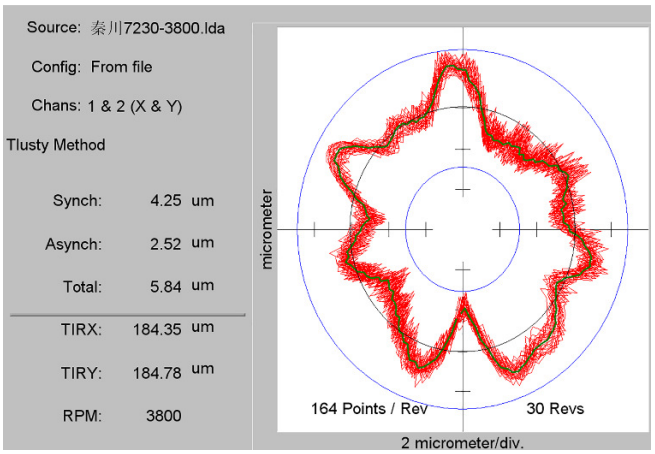

c)

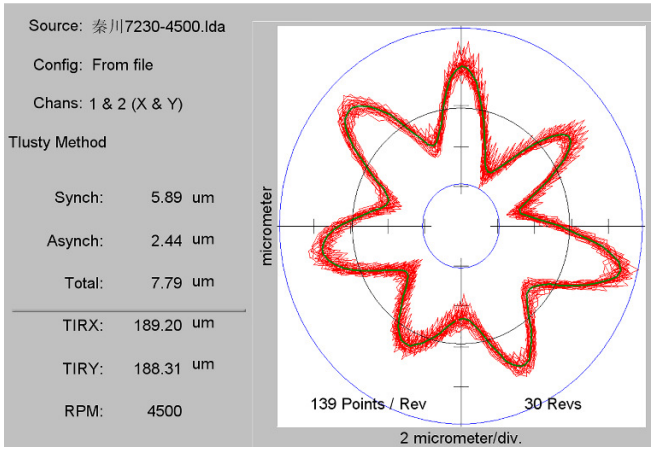

d)

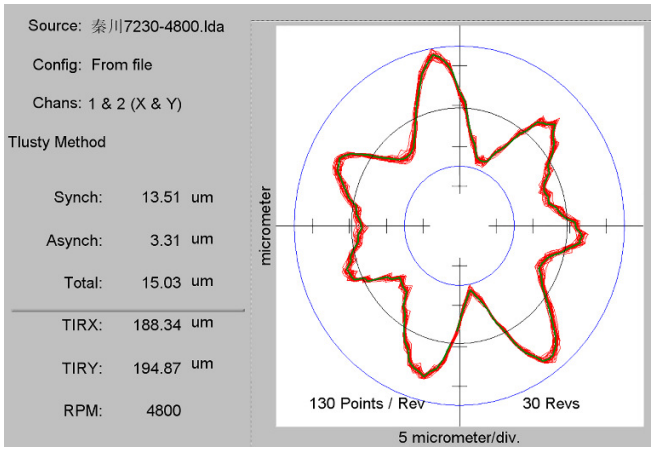

e)

Fig.19. Measured spindle trajectory a) n=3200 rpm, b) n=3600 rpm, c) n =3800 rpm, d) n=4500 rpm and e) n=4800 rpm.

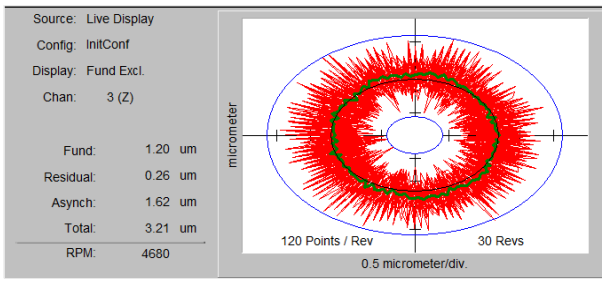

Fig.20. Measured Axial vibration at n=4680 rpm.

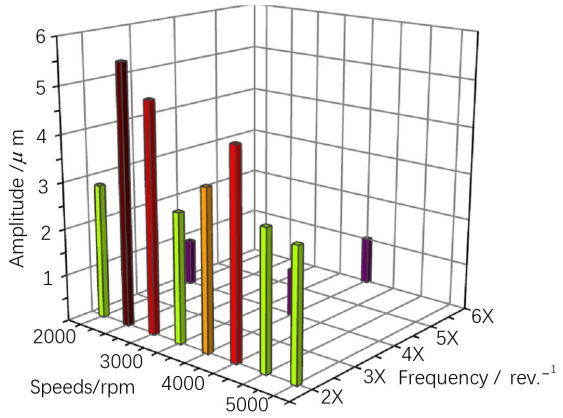

Fig.21. Measured vibration signals spectrum.

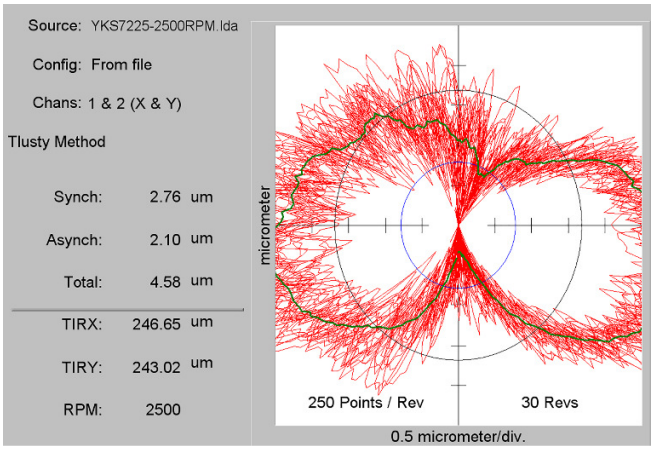

a)

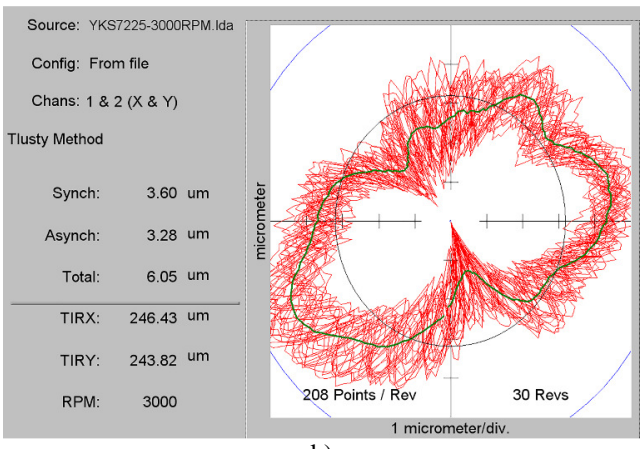

b)

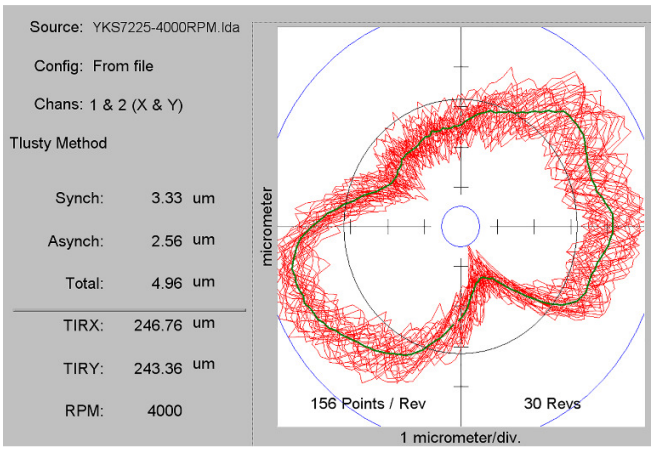

c)

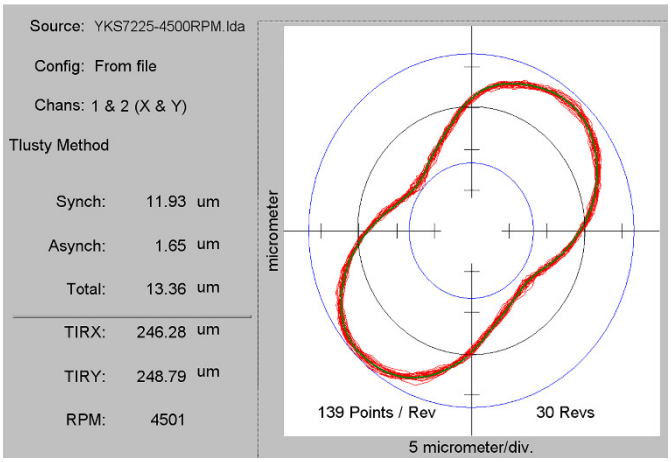

d)

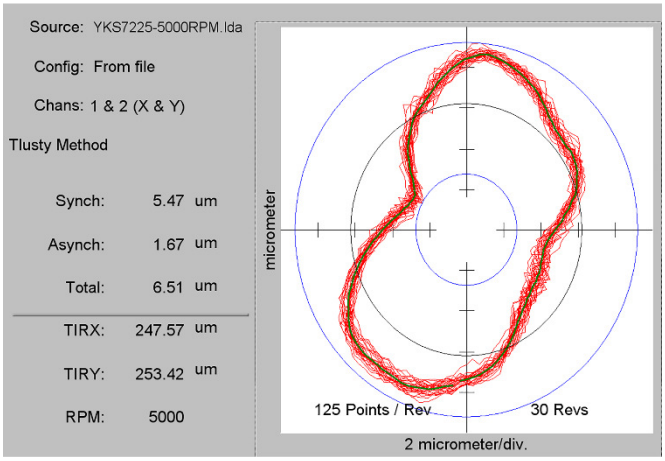

e)

Fig.22. Measured spindle trajectory a) n=2500 rpm, b) n=3000 rpm, c) n=4000 rpm, d) n=4500 rpm and e) n=5000 rpm.

The characteristic frequencies were measured at different speeds for the model YKS7225 motorized spindle. The speeds were n=2000 rpm, n=2500 rpm, n=3000 rpm, n=3500 rpm, n=4000 rpm, n=4500 rpm, n=5000 rpm, and n=5500 rpm, respectively. Fig.21. shows the spindle vibrations spectrum. From the spectrum results, it can be

asserted that the 2 rev.$^{-1}$, 4 rev.$^{-1}$, 6 rev.$^{-1}$ are the harmonics of 2 rev.$^{-1}$. Their amplitude gradually decreases and their maximum amplitude is 2 rev.$^{-1}$. The maximum amplitude of the vibration reaches 5.55 μm at n=4500 rpm. There were misalignment forced spindle vibrations induced by rotor. Therefore, it can be inferred that spindle tilting was quasi-elliptical. The spindle has both static and inclined eccentricity caused by the UMP due to manufacturing and assembling errors.

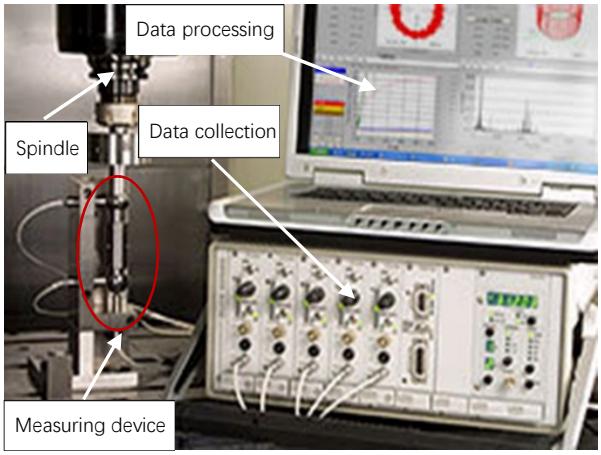

a)

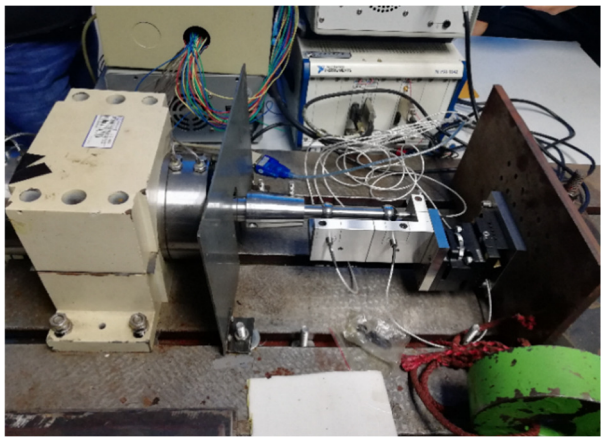

b)

Fig.23. Detecting the vibration of the spindle under high-speed operation a) in factory and b) in laboratory.

Fig.22. shows the measured trajectories for five different rotational speeds. In all cases, their maximum amplitude at the speed n=2500 rpm and the mass eccentricity was more obviously an effect of the spindle and the trajectorie's gradual transitions from approximately 8-shaped to near banana shape. The rotationally sensitive direction error increases from 4.58 μm to 13.36 μm, but decreases to 6.51 μm with increasing rotational speed. It is evident that at different rotational speeds there are UMP and mass eccentricity causing the spindle to be in the unstable subcritical region.

The vibration detection results of the proposed method can accurately identify the cause of the spindle vibrations. Double standard spheres for 5-DOF spindle vibration testing method can be applied not only to detect the radial vibration but also to detect the inclined vibration and the axial vibration.

Based on the above analysis, the proposed method can detect the dynamic characteristics of the spindle under high-speed operation. Fig.23. shows the vibration characteristics of the motorized spindle under high-speed operation in factory and laboratory. Therefore, the vibration detection and experimental method of spindle can predict the basis of vibration and fault diagnosis of motorized spindle.

6. Conclusions

We present a critical analysis, interpretation and evaluation of the obtained results. In this paper, a high-speed motorized spindle for a grinding machine tool was studied and the causes and vibration characteristics were analyzed. Based on the experimental modal analysis method, self-power spectrum and cross-power spectrum, the FRFs and the vibration spectrum were obtained. The least-square method was used to solve the radial trajectory of the spindle motion. The vibration spectrum was analyzed and double standard spheres for 5-DOF spindle vibration testing method were developed. The experimental study gives a better understanding of the spindle vibrations and its effect on the characteristic of the spindle so that the findings are achieved as follows:

1) Unbalanced magnetic pull (UMP) is one of the causes of the spindle vibrations and noises. In essence, the magnetic circuit or circuit asymmetry is the main reason for the generation of the UMP. The axes of the stator and rotor not being coincident are the most common cause of UMP. In addition, short circuit, open circuit, magnetization unevenness, and winding topology asymmetry can also result in UMP.

2) Bearings are the most common cause of mechanical vibrations. The ball-bearings supporting the spindle vibrations are categorized into three types, namely inner ring, outer ring, and ball damages. These vibrations affect the air–gap eccentricities which perturb flux density. Inertial effect and nonlinear Hertz contact force affect the motion of the spindle.

3) Double-standard sphere and displacement sensors are used to build an experimental platform and the vibration signals are collected at one time based on the mathematical models of the vibration detection. This paper used the MSSS-2556 testing system and the Lion non-contact capacitive displacement sensors to measure the displacement response of the spindle.

4) The spindle vibrational signal in FD and the trajectory are common tools in the spindle vibrations detection. The vibration detection results of the proposed method can accurately identify the cause of the spindle vibrations. Double standard spheres for 5-DOF spindle vibrations testing method can be applied not only to detect the radial vibration but also to detect the inclined vibration and the axial vibration. It is evident that the trajectory is different at different rotational speeds. The two methods verify each other during the vibration detection to ensure the accuracy compared with the experiment measured results. The proposed method can be used as the basis for the design and fault diagnosis of the motorized spindle.

ACKNOWLEDGMENT

This research was supported by the Natural Science Foundation of China (Grant No. 51775432). Shaanxi Key R&D Program（2018ZDXM-GY-074）.

REFERENCES

[1] Mehrjou, M.R. , Mariun, N. , Misron, N. , Radzi, M., Musa, S. (2017). Broken rotor bar detection in LS-PMSM based on startup current analysis using wavelet entropy features. *Applied Sciences*, 7 (8), 845.

[2] Xu, X., Han, Q., Chu, F. (2018). Review of electromagnetic vibration in electrical machines. *Energies*, 11 (7), 1779.

[3] Duan, Z., Wang, N., Fu, J., Zhao, W., Duan, B., Zhao, J. (2018). High precision edge detection algorithm for mechanical parts. *Measurement Science Review*, 18 (2), 65-71.

[4] Xiaohua, B., Lü, Q. (2013). Review and prospect of air-gap eccentricity faults in induction machines. *Proceedings of the CSEE*, 33 (6), 93-100. (in Chinese)

[5] Bruzzese, C. (2014). Diagnosis of eccentric rotor in synchronous machines by analysis of split-phase currents - Part I: Theoretical analysis. *IEEE Transactions on Industrial Electronics*, 61 (8), 4193-4205.

[6] Bruzzese, C. (2014). Diagnosis of eccentric rotor in synchronous machines by analysis of split-phase currents - Part II: Experimental analysis. *IEEE Transactions on Industrial Electronics*, 61 (8), 4206-4216.

[7] Torkaman, H., Afjei, E., Yadegari, P. (2012). Static, dynamic, and mixed eccentricity faults diagnosis in switched reluctance motors using transient finite element method and experiments. *IEEE Transactions on Magnetics*, 48 (8), 2254-2264.

[8] Wu, Y., Li, Y. (2016). Diagnosis of short circuit faults within turbogenerator excitation winding based on the expected electromotive force method. *IEEE Transactions on Energy Conversion*, 31 (2), 706-713.

[9] Zhang, G.T., Wu, J.Y., Hao, L.L. (2017). Fast calculation model and theoretical analysis of rotor unbalanced magnetic pull for inter-turn short circuit of field windings of non-salient pole generators. *Energies*, 10 (5), 732.

[10] Xie, Y., Zhang, T. (2015). A fault diagnosis approach using SVM with data dimension reduction by PCA and LDA method. In *Chinese Automation Congress (CAC)*, Wuhan, China. IEEE, 869-874.

[11] Glowacz, A. (2019). Fault diagnosis of the single-phase induction motor using acoustic signals. *Mechanical Systems and Signal Processing*, 117, 65-80.

[12] Gritli, Y., Rossi, C., Casadei, D., Filippetti, F., Capolino, G.A. (2017). A diagnostic space vector-based index for rotor electrical fault detection in wound-rotor induction machines under speed transient. *IEEE Transactions on Industrial Electronics*, 64 (5), 3892-3902.

[13] Ibrahim, R., Watson, S., Djurovic, S., Crabtree, C. (2018). An effective approach for rotor electrical asymmetry detection in wind turbine DFIGs. *IEEE Transactions on Industrial Electronics*, 65 (11), 8872 - 8881.

[14] Youn, Y.W., Hwang, D.H., Song, S.J., Kim, Y.H. (2018). Detection and classification of demagnetization and short-circuited turns in permanent magnet synchronous motors. *Journal of Electrical Engineering & Technology*, 13 (4), 1613-1621.

[15] Chandra, N.H., Sekhar, A.S. (2016). Fault detection in rotor bearing systems using time frequency techniques. *Mechanical Systems & Signal Processing*, 72-73, 105-133.

[16] Li, H., Li, M., Li, C., Li, F., Meng, G. (2017). Multi-faults decoupling on turbo-expander using differential-based ensemble empirical mode decomposition. *Mechanical Systems and Signal Processing*, 93, 267-280.

[17] Ebrahimi, R., Ghayour, M., Khanlo, H.M. (2018). Nonlinear dynamic analysis and experimental verification of a magnetically supported flexible rotor system with auxiliary bearings. *Mechanism and Machine Theory*, 121, 545-562.

[18] Guo, D., Chu, F., Chen, D. (2002). The unbalanced magnetic pull and its effects on vibration in a three-phase generator with eccentric rotor. *Journal of Sound and Vibration*, 254 (2), 297-312.

[19] Xiang, C., Liu, F., Liu, H., Han, L., Zhang, X. (2016). Nonlinear dynamic behaviors of permanent magnet synchronous motors in electric vehicles caused by unbalanced magnetic pull. *Journal of Sound & Vibration*, 371, 277-294.

[20] Jiang, J.W., Sathyan, A., Dadkhah, H., Bilgin, B., Emadi, A. (2016). Analysis of unbalanced magnetic pull in eccentric interior permanent magnet machines with series and parallel windings. *IET Electric Power Applications*, 10 (6), 526-538.

[21] Di, C., Bao, X., Wang, H., Lv, Q., He, Y. (2015). Modeling and analysis of unbalanced magnetic pull in cage induction motors with curved dynamic eccentricity. *IEEE Transactions on Magnetics*, 51 (8), 8106507.

[22] Xianguang, L., Yong, Y. (2017). Research on the vibration properties of hob spindle for CNC gear hobbing machine. *Journal of Mechanical Engineering*, 53 (1), 130-139. (in Chinese)

[23] Amirat, Y., Benbouzid, M.E.H., Bensaker, B., Wamkeue, R. (2007). Condition monitoring and ault diagnosis in wind energy conversion systems: A review. In *IEEE International Electric Machines & Drives Conference*, Antalya, Turkey. IEEE, 1434-1439.

[24] Liu, C.Y., Zheng, F., Wang, L.P. (2018) Vibration transmission mechanical model between the shaft and housing of a high speed motor spindle. *Journal of Tsinghua University (Science and Technology)*, 58 (7), 671-676. (in Chinese)

[25] Xu, X., Han, Q., Chu, F. (2018). A general electromagnetic excitation model for electrical machines considering the magnetic saturation and rub impact. *Journal of Sound and Vibration*, 416, 154-171.
[26] Gu, Y., Ma, Y., Ren, G. (2017). Stability and vibration characteristics of a rotor-gas foil bearings system with high-static-low-dynamic-stiffness supports. *Journal of Sound & Vibration*, 397, 152-170.
[27] Miraskari, M., Hemmati, F., Gadala, M.S. (2017). Nonlinear dynamics of flexible rotors supported on journal bearings - Part I: Analytical bearing model. *Journal of Tribology*, 140 (2), 021704.
[28] Miraskari, M., Hemmati, F., Gadala, M.S. (2017). Nonlinear dynamics of flexible rotors supported on journal bearings - Part II: Numerical bearing model. *Journal of Tribology*, 140 (2), 021705.
[29] Han, X., Palazzolo, A. (2016). Unstable force analysis for induction motor eccentricity. *Journal of Sound & Vibration*, 370, 230-258.
[30] Yu-Ling, H., Wei-Qi, D., Bo, P., Meng-Qiang, K., Gui-Ji, T., Shu-Ting, W. (2016). Stator vibration characteristic identification of turbogenerator among single and composite faults composed of static air-gap eccentricity and rotor interturn short circuit. *Shock and Vibration*, 2016, 5971081.
[31] Hawwooi, C., Shek, J.K.H. (2018). Calculation of unbalanced magnetic pull in induction machines through empirical method. *IET Electric Power Applications*, 12 (9),1233-1239.
[32] Bai, Y., Yang, B., Li, H. (2018). Analysis of nonlinear vibration in permanent magnet synchronous motors under unbalanced magnetic pull. *Applied Sciences*, 8 (1), 113.
[33] Li, Y.X., Zhu, Z.Q. (2017). Cogging torque and unbalanced magnetic force prediction in pm machines with axial-varying eccentricity by superposition method. *IEEE Transactions on Magnetics*, 53 (11), 1400404.
[34] Megha, S., Abdul, G.S. (2019). Faulty bearing detection, classification and location in a three-phase induction motor based on Stockwell transform and support vector machine. *Measurement*, 131, 524-533.
[35] Zhang, S.J., Yu, J.J., To, S., Xiong, Z.W. (2018). A theoretical and experimental study of spindle imbalance induced forced vibration and its effect on surface generation in diamond turning. *International Journal of Machine Tools & Manufacture*, 133, 61-71.
[36] Anandan, K.P., Ozdoganlar, O.B. (2013). Analysis of error motions of ultra-high-speed (UHS) micromachining spindles. *International Journal of Machine Tools and Manufacture*, 70, 1-14.
[37] Zhang, P., Chen, Y. (2018). Analysis of error motions of axial locking-prevention hydrostatic spindle. *Proceedings of the Institution of Mechanical Engineers, Part J: Journal of Engineering Tribology*, 233 (1), 3-17.
[38] Nishiguchi, T., Sato, R., Shirase, K. (2017). Evaluation of axial displacement caused by rotary axis motion direction change in five-axis controlled machining centers. *Journal of the Japan Society for Precision Engineering*, 83 (9), 893-898.
[39] Huang, S., Huang, K., Chao, K. (2016). Fault analysis and diagnosis system for induction motors. *Computers & Electrical Engineering*, 54, 195-209.

Received November 29, 2018
Accepted May 30, 2019